Research Square

Preprints are preliminary reports that have not undergone peer review.
They should not be considered conclusive, used to inform clinical practice,
or referenced by the media as validated information.

Conductivity Effects on the Thermal Performance of Plate-Fin Heat Sinks

Bernardo Piteira

bernardo.piteira@ubi.pt

University of Beira Interior

Luís Calmeiro

University of Beira Interior

Francisco Brójo

University of Beira Interior

Research Article

Keywords:

Posted Date: November 4th, 2026

DOI: https://doi.org/10.21203/rs.3.rs-11244269/v1

License: This work is licensed under a Creative Commons Attribution 4.0 International License.
Read Full License

Additional Declarations: No competing interests reported.

Conductivity Effects on the Thermal Performance of Plate-Fin Heat Sinks

Bernardo Piteira[a,*], Luís Calmeiro[a], Francisco Brójo[b]

[a] *Department of Aerospace Sciences, Universidade da Beira Interior, Covilhã, Portugal*
[b] *Center for Mechanical and Aerospace Science and Technologies (C-MAST-UBI), University of Beira Interior, R. Marquês de D'Ávila e Bolama, 6201-001 Covilhã, Portugal*

Abstract

The forced convection heat transfer characteristics of plate-fin heat sinks are numerically investigated to evaluate the explicit influence of substrate material selection on thermal performance. Locking the physical geometry into a uniform heating profile ($L_h/L = 1.0, L_c/L = 0.5$), a high-fidelity 3D Conjugate Heat Transfer (CHT) CFD framework is developed to resolve the simultaneous coupling between solid conduction and fluid convection. A structured Hexcore mesh is utilized to capture complex solid-fluid boundary layer interactions across multiple volumetric flow rates ($Q = 0.2$ to 0.8 m^3/min). The numerical results demonstrate that utilizing high-conductivity materials significantly suppresses downstream thermal accumulation, lowering peak operating temperatures compared to low condutivity materials like titanium or stainless steel, for example. Furthermore, the 3D model identifies a critical transition threshold where expanding the airflow rate yields diminishing returns as the system shifts from a convection-limited domain to a conduction-bound regime dictated entirely by the material's bulk thermal conductivity (k). These findings establish vital thermodynamic selection criteria for the material and structural optimization of advanced high-power electronic cooling configurations.

Keywords: Plate-fin heat sink; Material selection; Thermal conductivity; Forced convection; Conjugate Heat Transfer (CHT); 3D CFD simulation.

1. Introduction

The exponential increase in power densities within modern electronic packages requires highly efficient thermal management strategies to prevent component failure and ensure operational reliability Incropera et al. (2011). Plate-fin heat sinks under forced convection remain a cornerstone technology for localized heat removal. However, selecting an appropriate structural material is as critical as geometric optimization. The global efficiency of a cooling system is governed by a complex thermodynamic balance between internal solid conduction and external fluid convection.

While rapid analytical frameworks often assume an idealized isothermal substrate base, real engineering applications suffer from internal thermal resistance within the solid block, leading to structural performance bottlenecks. The primary objective of this work is to extend the geometric and spatial optimization findings established in our previous study Piteira and Calmeiro (2026). While our prior work characterized the impact of localized heating positions and fin densities using a baseline stainless steel substrate, it highlighted a distinct physical transition toward a conduction-limited domain at higher flow rates. To address this specific limitation, the present paper locks the computational domain into a high-density 25-fin geometry under uniform full heating ($L_h/L = 1.0$, $L_c/L = 0.5$) to isolate and evaluate the explicit thermodynamic impact of alternative substrate core materials.

2. Literature Review

The modeling of thermal transport across physical boundaries requires an exact characterization of solid-fluid coupling, a phenomenon formally resolved through 3D Conjugate Heat Transfer (CHT) numerical approaches, as demonstrated by Piteira et al. Piteira and Calmeiro (2026) under partial heating dynamics. CHT methodologies solve the coupled conservation of energy equations simultaneously across solid domains and fluid interfaces, capturing the true multi-directional conduction pathways that standard empirical models typically neglect.

The explicit optimization of air-cooled geometries under specialized configurations has been heavily detailed in traditional investigations. In classical plate-fin research, such as the experimental benchmarks by Lee et al. Lee et al. (2019), spatial thermal sensitivities are typically mapped using standard high-resistance alloys. They established that for laminar developing flows, partial heat deposition closer to the upstream boundary significantly minimizes absolute thermal accumulation compared to downstream positions. To extend these configurations into high-performance domains, recent structural investigations have explored flow-disrupting inserts.

*Corresponding authors.
Email address: bernardo.piteira@ubi.pt (Bernardo Piteira)

To extend these configurations into high-performance domains, recent structural investigations have explored flow-disrupting inserts. For instance, advanced numerical and experimental assessments of plate-fin arrays by Shyu and Jheng Shyu and Jheng (2020) have proven that generating targeted winglet vortex structures and altering local fluid flow profiles can significantly enhance convective heat transfer, delivering substantial reductions in global thermal resistance compared to un-optimized boundary layer conditions.

However, scaling the physical dimensions or material properties of the substrate base is tightly governed by clear thermodynamic saturation boundaries. Numerical evaluations by Lim et al. Lim et al. (2026) focusing on the explicit sensitivity of base substrate materials have shown that while increasing thermal conductivity (k) monotonically enhances heat dissipation, this optimization tracks asymptotically toward a predictable upper limit. Beyond a threshold matching high-conductivity metals like gold, copper, or silver, any further inflation of the substrate's bulk conductivity ceases to yield measurable enhancements, matching the performance of a theoretically infinite conductive base as the system transitions into a strict convection-limited external bottleneck.

When a heat sink is fully heated, a stream-wise thermal boundary layer develops along the internal flow channels, progressively degrading the local convective heat transfer coefficient downstream. To mitigate this continuous temperature accumulation, the structural substrate must possess high thermal conductivity (k) to spread the heat backward against the core flow direction. Recent literature highlights that as volumetric flow rates (Q) increase, the convective thermal resistance within the fluid drops significantly, causing the internal conductive resistance of the solid block to become the dominant thermal constraint.

Complementing these geometric enhancements, the interaction between structural mass reduction and thermal efficacy remains a key paradigm in high-power systems. In an evaluation of natural and forced convection cooling parameters, Culham et al. Culham et al. (2007) demonstrated that while localized spreading resistance dominates thin substrates, optimized fin aspect ratios can partially compensate for the lower thermal conductivity of alternative materials. Furthermore, recent numerical assessments of surface modification techniques by Lim et al. Lim et al. (2026) highlighted that applying high-emissivity composite coatings over variable metallic heat sink layouts selectively enhances passive radiative heat loss without introducing convective degradation.

3. Problem Statement and Geometry

To isolate and analyze the explicit thermodynamic impact of substrate material properties on localized cooling performance, this study investigates forced convection over a fixed high-density plate-fin heat sink layout. The baseline geometry is validated against the experimental domain described by Lee et al. Lee et al. (2019). A schematic of the physical heat sink block under a uniform thermal configuration is illustrated in Fig. 1. The cooling airflow within the inter-fin channels operates under a developing laminar regime.

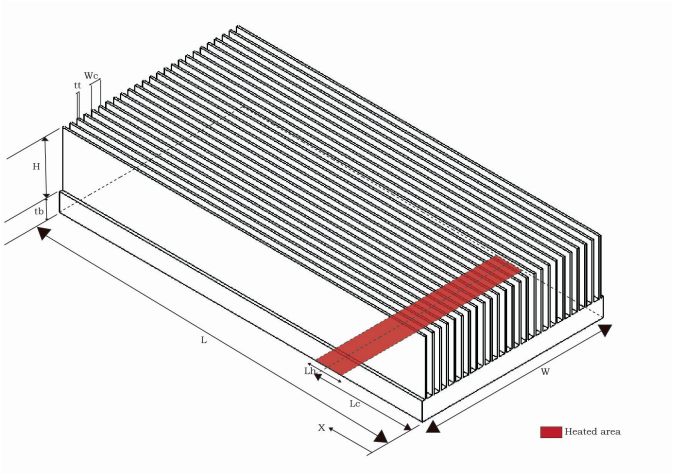


Figure 1: Schematic representation of the plate-fin heat sink layout and the localized partial heating zones along the base.

To systematically evaluate metallurgical variances without geometric cross-coupling, the computational setup is strictly locked into the $N = 25$ fins layout subjected to a full uniform base heating profile ($L_h/L = 1.0$, $L_c/L = 0.5$). The fixed geometric parameters characterizing this solid domain are detailed in Table 1.

Table 1: Fixed geometric characteristics of the 25-fin heat sink.

Geometric Parameter	**Value**
Number of Fins (N)	25
Channel Width (w_c, mm)	3
Length (L, mm)	200
Width (W, mm)	100
Height (H, mm)	30
Base Thickness (t_b, mm)	10
Fin Thickness (t_f, mm)	1

The primary focus of this numerical investigation is the comparative evaluation of eleven alternative metal matrices and commercial engineering alloys. The temperature-independent isotropic thermophysical properties utilized to parameterize the solid heat sink domains are compiled in Table 2.

To ensure strict numerical and empirical validity, the fundamental properties for the pure metal matrices (Silver, Copper, Gold, and Aluminum 1050) were extracted from the standardized reference data provided by Incropera et al. Incropera et al. (2011). To

complement the analysis with standard aerospace and industrial metallurgy, the structural and chemical engineering profiles for the complex alloys—specifically Aluminum 6061-T6, Brass C360, Carbon Steel 1020, and Stainless Steel 304—were validated using the comprehensive engineering datasheets retrieved from the MatWeb Materials Property Database Automation Creations, Inc. (2026). The advanced operational specifications for the grade 5 titanium alloy (Ti-6Al-4V) and the nickel-chromium superalloy (Inconel 718) were cross-referenced with the verified SolidWorks Materials Library Das (2026).

Table 2: Thermophysical properties and data sources of the evaluated substrate metals.

Alloy / Metal Name	**k** (W/m·K)	ρ (kg/m^3)	$\mathbf{C_p}$ (J/kg·K)	**Data Source**
Pure Silver	429.0	10490	235	Incropera Incropera et al. (2011)
Copper C101	401.0	8933	385	Incropera Incropera et al. (2011)
Pure Gold	317.0	19300	129	Incropera Incropera et al. (2011)
Aluminum 1050	231.0	2705	900	Incropera Incropera et al. (2011)
Aluminum 6061-T6	167.0	2700	896	MatWeb Automation Creations, Inc. (2026)
Magnesium AZ91D	156.0	1810	1020	SolidWorks Das (2026)
Brass C360	115.0	8500	380	MatWeb Automation Creations, Inc. (2026)
Carbon Steel 1020	52.0	7870	486	MatWeb Automation Creations, Inc. (2026)
Stainless Steel 304	16.2	8000	502	MatWeb Automation Creations, Inc. (2026)
Inconel 718	11.4	8190	435	SolidWorks Das (2026)
Titanium Ti-6Al-4V	6.7	4430	526	SolidWorks Das (2026)

This extensive metallic matrix spans an operational thermal conductivity range from $k = 429.0$ W/m·K down to $k = 6.7$ W/m·K, establishing the necessary computational boundary conditions to analyze the mathematical transition from convection-limited fluid paths to solid conduction-bound structures. A constant and uniform thermal load of $q = 40$ W is applied across the entire base area. To evaluate the fluid dynamic behavior and cooling efficiency under varying operational parameters, the parametric variations are carried out across four distinct volumetric airflow rates (Q), as mapped in Table 3.

Table 3: Parametric matrix for the material analysis case study.

$\mathbf{L_h/L}$	$\mathbf{L_c/L}$	**Q** (m^3/min)
1.0	0.5	0.2, 0.4, 0.6, 0.8

To replicate wind tunnel containment and prevent unconstrained fluid bypass flow—which would suppress convective cooling effects—the computational enclosure restricts the fluid margins. The full layout showing wall clearance margins is illustrated in Fig. 2. These strict clearance metrics are summarized in Table 4.

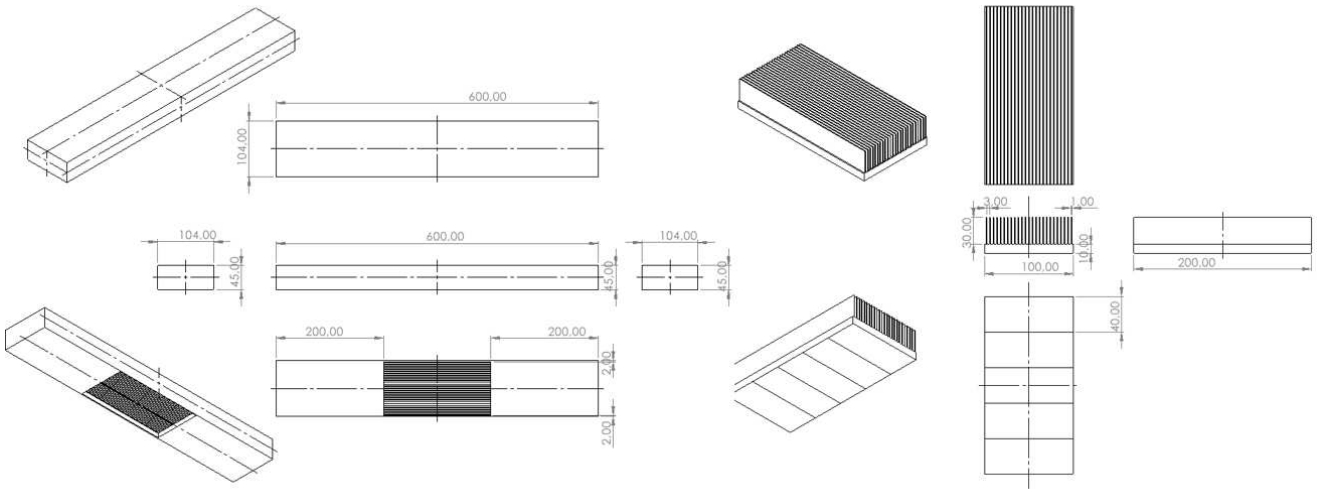


Figure 2: Computational geometry.

Table 4: Computational fluid domain clearance constraints.

Domain Boundary Wall	Clearance Distance (mm)
Left Wall (L_W)	2
Right Wall (R_W)	2
Top Wall (T_W)	5
Bottom Wall (B_W)	0
Front Extension (F_W)	200
Back Extension ($Back_W$)	200

The governing mathematical framework simultaneously solves the incompressible Navier-Stokes equations within the fluid domain and the 3D solid heat conduction equation inside the selected metal blocks. The matching boundary conditions prescribed across the computational boundaries dictate a uniform velocity profile at the air flow inlet, a pressure outlet constraint at the downstream fluid face, and a uniform heat flux condition modeling the electronic load at the lower base interface. All remaining structural exterior boundaries are treated as adiabatic.

4. Numerical Mesh and Grid Independence Study

4.1. Mesh Topology and Interface Discretization

The spatial discretization of the computational solid block and the fluid bounding margins for the $N = 25$ fin configuration was executed utilizing a hybrid Poly-Hexcore multi-block strategy. To optimize processing times and accelerate convergence rates, the core fluid domain inside the inter-fin channels is resolved with structured hexahedral cells. The geometric transition between the inner channel surfaces and the exterior freestream environment is bridged via specialized polyhedral cells.

To resolve the intense velocity and thermal boundary layers developed along the cooling tracks, a refined surface mesh with a target cell sizing of 2 mm was prescribed across the solid interfaces, as visualized in Fig. 3. To prevent numerical diffusion errors across the Conjugate Heat Transfer (CHT) boundary, four structured inflation layers were placed at the fluid-solid walls. The mesh quality statistics verified for the selected validation grid are summarized in Table 5.

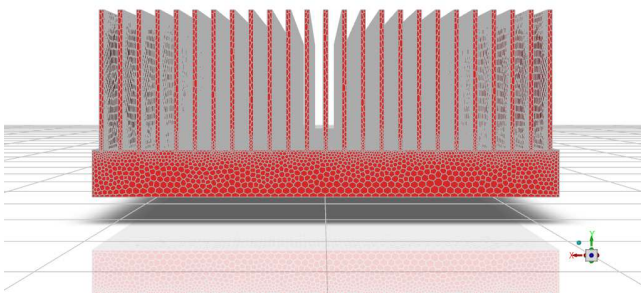


Figure 3: Numerical mesh topology and boundary layer refinement zones over the selected 25-fin plate-fin geometry.

Table 5: Grid statistics and quality parameters for the production N25 mesh.

Quality Metric	25-Fin Layout Value
Total Element Count	422,875
Average Skewness	0.11066
Maximum Skewness	0.63772
Average Orthogonal Quality	0.88448
Minimum Orthogonal Quality	0.20028
Average Aspect Ratio	3.01240

4.2. Grid Convergence Verification

To mathematically guarantee that the spatial grid density does not compromise the numerical precision of the solutions, a systematic grid independence study was performed. The validation benchmark was locked on the 25-fin configuration operating at a baseline volumetric airflow rate of $Q = 0.2$ m^3/min. The control variable tracked across successive refinements was the area-weighted average temperature of the heat sink base substrate ($T_{\text{base, avg}}$).

Three independent grid configurations—Coarse, Medium, and Fine—were tested. The numerical convergence behavior and relative errors (ϵ_{rel}) computed via successive step deviations are detailed in Table 6.

Table 6: Mesh independence validation parameters for the N25 geometry.

Mesh Level	Elements	$\mathbf{T}_{\text{base, avg}}$ (K)	ϵ_{rel} (%)
Coarse	165,420	316.8541	—
Medium	422,875	315.5088	0.320
Fine	1,125,640	315.4593	0.016

The transition from the Coarse mesh to the Medium grid captures the sharp fluid gradients, resulting in a temperature stabilization shift. Further refinement to the Fine mesh level yields a residual deviation of only 0.05 K ($\epsilon_{\text{rel}} = 0.016\%$).

Because the stabilization deviation sits well below the strict solver stop threshold (< 0.1 K), the Medium mesh featuring 422,875 elements was selected as the optimal production grid, balancing physical accuracy with numerical computation economy.

5. Results and Discussion

5.1. Thermal Profile Analysis and Model Validation

The numerical Conjugate Heat Transfer (CHT) simulations were evaluated by extracting the continuous local temperature profiles ($\Delta T = T_b - T_{amb}$) along the central longitudinal axis (x-coordinate) of the heat sink base substrate. To analyze metallurgical variables without geometric cross-coupling, the thermal fields were systematically mapped across all eleven alternative metallic substrates under multiple discrete volumetric flow rates (Q).

The longitudinal temperature distribution operating at the baseline flow rate of $Q = 0.2$ m^3/min is graphically illustrated in Fig. 4. Across all evaluated configurations, the local thermal fields exhibit a progressive stream-wise temperature rise from the inlet boundary ($x = 0.00$ m) toward the trailing exit edge ($x = 0.20$ m). This continuous thermal acceleration is a direct physical consequence of the development of the laminar thermal boundary layer inside the 25-fin channels, which thickens downstream and degrades the local convective heat transfer coefficient.

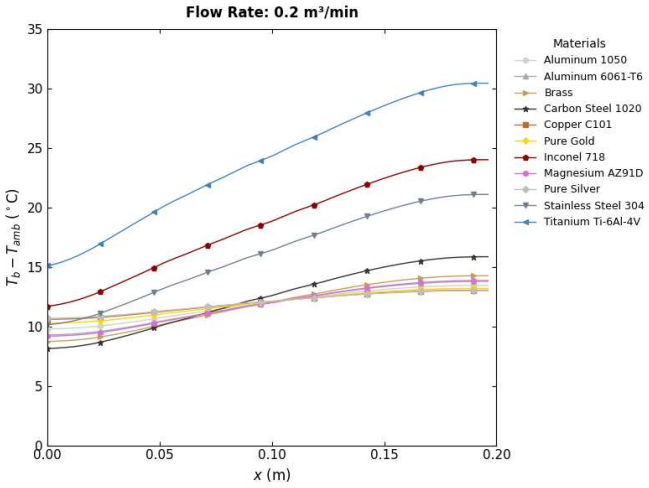


Figure 4: Longitudinal base temperature profiles (ΔT) for the eleven alternative metallic substrates operating at a volumetric flow rate of $Q = 0.2$ m^3/min.

The conjugate numerical solution at $Q = 0.2$ m^3/min reveals a severe performance bifurcation dictated strictly by the substrate's bulk thermal conductivity (k). High-conductivity matrices—encompassing Pure Silver, Copper C101, Pure Gold, Aluminum 1050, Aluminum 6061-T6, and Magnesium AZ91D—cluster densely at the lower envelope of the domain, clamping the maximum thermal peak between 13°C and 14°C. The high isotropic conduction inside these structural blocks flattens local gradients via multi-directional heat spreading through the solid base.

Conversely, low-conductivity structural alloys experience an extreme localized thermal penalty. Inconel 718 ($k = 11.4$ W/m·K) and Titanium Ti-6Al-4V ($k = 6.7$ W/m·K) restrict internal conduction pathways, causing severe energy accumulation. The titanium substrate baseline drives the local trailing temperature up to a critical peak of 30.5°C, representing

a substantial hot spot amplification.

5.2. Thermal Evolution under Enhanced Advection

When the volumetric airflow rate is scaled to $Q = 0.4$ m^3/min, as plotted in Fig. 5, an aggressive global temperature suppression manifests across all configurations. This downward shift mathematically validates the scaling of the convective heat transfer coefficient (h) triggered by the thinning of the fluid boundary layers.

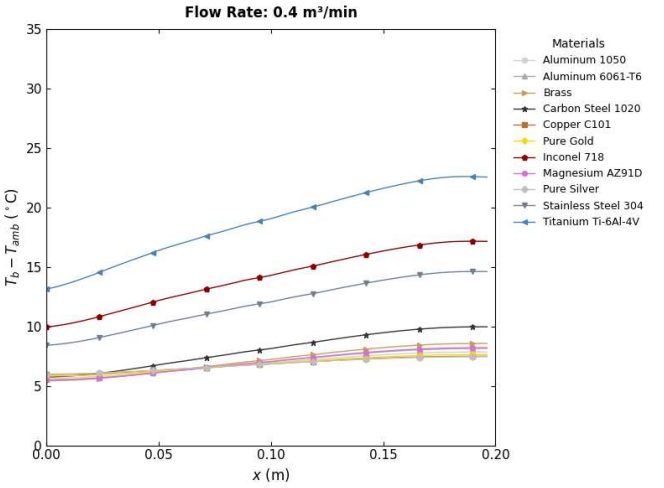


Figure 5: Longitudinal base temperature profiles (ΔT) for the eleven alternative metallic substrates operating at an increased flow rate of $Q = 0.4$ m^3/min.

The maximum thermal peak experienced by the Titanium Ti-6Al-4V substrate drops substantially from 30.5°C to 22.6°C, representing a 25.9% reduction in hot spot intensity driven solely by fluid advection. For the high-conductivity cluster, the thermal profiles become remarkably uniform, stabilizing at a tight maximum baseline range between 7.5°C and 8.5°C, shifting the dominant cooling bottleneck away from the solid block.

Scaling the volumetric airflow rate further to $Q = 0.6$ m^3/min, as illustrated in Fig. 6, reveals a critical physical transition in the cooling mechanics. While lower-conductivity alloys continue to show noticeable peak temperature drops—with the titanium maximum decreasing down to 19.4°C—the high-conductivity metallic matrix experiences a distinct performance saturation.

For substrate metals such as Pure Silver, Copper C101, and the commercial Aluminum alloys, the maximum base temperature clamping profile registers a minimal decrease, stabilizing tightly within the narrow margin of 5.5°C to 6.5°C. This behavior demonstrates the physical onset of diminishing returns re-

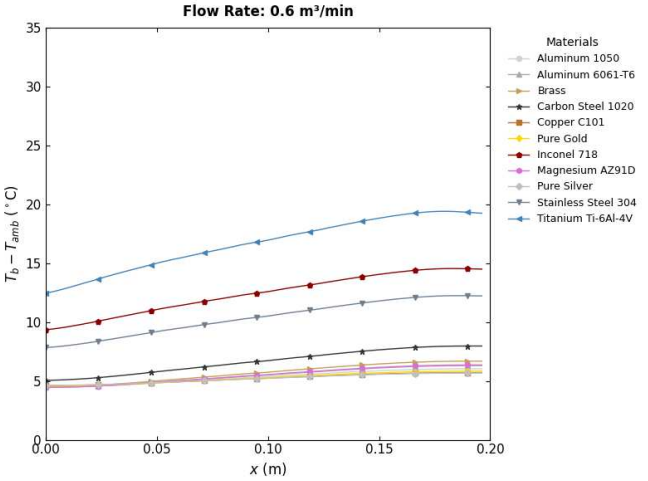


Figure 6: Longitudinal base temperature profiles (ΔT) for the eleven alternative metallic substrates operating at a high flow rate of $Q = 0.6$ m^3/min.

garding fluid dynamic scaling, indicating that the layout has transitioned into a strict conduction-bound regime.

This asymptotic trend is consolidated at the maximum evaluated airflow velocity of $Q = 0.8$ m^3/min, as depicted in Fig. 7. The high-conductivity cluster remains entirely clamped within a baseline delta window between 4.5°C and 5.5°C, rendering the thermal profiles nearly identical despite massive differences in their material densities.

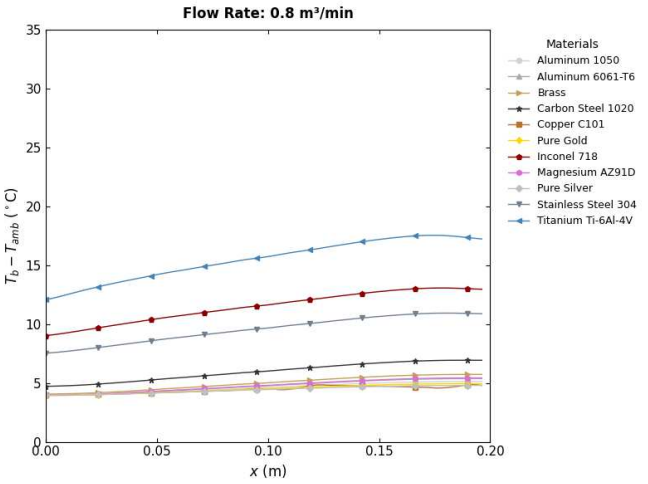


Figure 7: Longitudinal base temperature profiles (ΔT) for the eleven alternative metallic substrates operating at the maximum flow rate of $Q = 0.8$ m^3/min.

At this high-flow velocity threshold, the external convective thermal resistance inside the 25-fin voids has been suppressed to values close to zero. Consequently, the global heat transfer path is completely

throttled by the internal thermal conduction capacity of the 10 mm substrate solid block, making geometric optimization secondary to structural alloy selection.

5.3. Global Thermal Resistance and Weight Optimization

The global parametric overview evaluating the absolute thermal resistance (R) across all eleven alternative metallic substrates is summarized in the comprehensive comparative bar chart in Fig. 8. The quantitative distribution establishes that at lower velocities ($Q = 0.2$ m^3/min), traditional high-performance matrices such as Pure Silver ($k = 429.0$ W/m·K) and Copper C101 ($k = 401.0$ W/m·K) exhibit the lowest overall thermal resistance values, quantified at approximately 0.33 K/W.

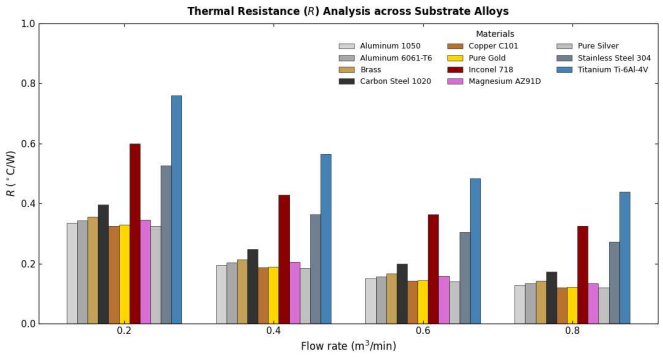


Figure 8: Global thermal resistance (R) comparison across the eleven evaluated substrate metals as a function of volumetric airflow rate (Q).

Conversely, Titanium Ti-6Al-4V drives the global thermal resistance up to a peak value of 0.76 K/W, representing a severe performance degradation of over 130% compared to the copper baseline due to its internal conductive blockages.

From an advanced aerospace optimization standpoint, while pure precious metals minimize absolute temperature fields, commercial Aluminum 1050 ($k = 231.0$ W/m·K) achieves a nearly identical thermal profile to copper while providing a 69.7% reduction in total component mass due to its lightweight density ($\rho = 2705$ kg/m^3). This balances thermodynamic requirements with aircraft structural constraints, identifying lightweight aluminum matrices as the optimal selection criteria for airborne power electronics integration.

6. Conclusion

This study systematically evaluated the forced convection heat transfer characteristics of a high-density 25-fin plate-fin heat sink subjected to uniform full heating ($L_h/L = 1.0, L_c/L = 0.5$) by evaluating eleven alternative metallic substrates through a high-fidelity 3D Conjugate Heat Transfer (CHT) framework. The continuous fluid-solid thermal coupling resolved within the computational domains provided critical insights into the physical mechanisms governing material-bound electronic cooling.

Metallurgical Impact on Thermal Uniformity: The comparative analysis between pure metals and commercial engineering alloys demonstrated that core substrate thermal conductivity (k) plays a paramount role in temperature uniformity and hot spot mitigation. Utilizing high-conductivity substrates, such as Pure Silver ($k = 429.0$ W/m·K) and Copper C101 ($k = 401.0$ W/m·K), significantly suppresses downstream heat accumulation along the inter-fin channels, lowering absolute operating peak values and flattening the solid base temperature profiles compared to high-resistance alloys like Titanium Ti-6Al-4V ($k = 6.7$ W/m·K) and Inconel 718 ($k = 11.4$ W/m·K).

Conduction-Convection Threshold Transition: The parametric flow variations identified a critical physical transition boundary when scaling the volumetric airflow rate (Q) from 0.2 to 0.8 m^3/min. At lower velocities, convective scaling dominates the global heat dissipation rate, providing substantial cooling increments across all configurations. However, at higher volumetric thresholds, the external convective thermal resistance inside the fluid channels drops near zero, causing the internal conductive resistance of the metal block to become the primary thermodynamic bottleneck. This leads to severe diminishing returns for high-conductivity substrates, shifting the system into a strict conduction-bound regime where the material's bulk conductivity acts as the absolute operational limit.

Aerospace Performance-to-Weight Optimization: From an advanced airborne structural packaging perspective, minimizing absolute temperature fields must be balanced against component mass constraints. While pure precious metals minimize thermal fields, commercial Aluminum 1050 ($k = 231.0$ W/m·K) and Aluminum 6061-T6 ($k = 167.0$ W/m·K) achieve thermal resistance profiles nearly identical to the copper baseline while providing a 69.7% reduction in total component weight due to their lightweight densities ($\rho \approx 2700$ kg/m^3). This balance identifies lightweight aluminum matrices as the optimal selection criteria for airborne power electronics integration.

Ultimately, these numerical findings extend the spa-

tial geometry optimization established in our companion study Piteira and Calmeiro (2026). They demonstrate that proper structural material selection is essential to fully exploit fluid dynamic advancements and achieve effective thermal management in next-generation high-power electronics packages.

Conflict of Interest

The authors declare no conflict of interest.

CRediT authorship contribution statement

Bernardo Piteira: Conceptualization, Numerical methodology, MATLAB algorithm development, CFD simulation framework, Writing – original draft.

Luís Calmeiro: Data analysis, Grid verification sweeps, Writing – review & editing.

Francisco Brójo: Conceptualization, Funding acquisition, Investigation, Project administration, Resources, Software, Supervision, Validation, Writing – review & editing.

Declaration of competing interest

The authors declare that they have no known competing financial interests or personal relationships that could have appeared to influence the work reported in this paper.

Acknowledgment

The authors acknowledge the support granted by the Research Unit of Centre for Mechanical and Aerospace Science and Technologies (C-MAST-UBI), through the Projects references UID/00151/2025 (https://doi.org/10.54499/UID/00151/2025), UID/PRR/00151/2025 (https://doi.org/10.54499/UID/PRR/00151/2025) and UID/PRR2/00151/2025(https://doi.org/10.54499/UID/PRR2/00151/2025), funded by FCT - Fundação para a Ciência e a Tecnologia, IP/MECI.

References

F. P. Incropera, D. P. DeWitt, T. L. Bergman, and A. S. Lavine. *Fundamentals of Heat and Mass Transfer*. John Wiley & Sons, 7th edition, 2011.

B. Piteira and L Calmeiro. Conjugate heat transfer analysis of plate-fin heat sinks under partial heating conditions. 2026. Preprint / Companion study.

J. J. Lee, H. J. Kim, and D.-K. Kim. Experimental study on forced convection heat transfer from plate-fin heat sinks with partial heating. *Processes*, 7(10): 772, 2019. doi: 10.3390/pr7100772.

Jin-Cherng Shyu and Jhao-Siang Jheng. Heat transfer enhancement of plate-fin heat sinks with different types of winglet vortex generators. *Energies*, 13(19): 5219, 2020. doi: 10.3390/en13195219.

Xing Qi Lim, Mohd Sharizal Abdul Aziz, C. Y. Khor, and Janter Pangaduan Simanjuntak. Influence of heat sink material and surface coatings on passive cooling thermal performance. *Journal of Electronic Materials*, 55(4):1522–1536, 2026. doi: 10.1007/s11664-025-12284-w.

J. Richard Culham, Waqar A. Khan, M. Michael Yovanovich, and Yuri S. Muzychka. The influence of material properties and spreading resistance in the thermal design of plate fin heat sinks. *Journal of Electronic Packaging*, 129(1):76–81, 2007. doi: 10.1115/1.2429713.

Automation Creations, Inc. Matweb: Online materials information resource. https://matweb.com, 2026. Accessed: June 23, 2026.

SolidWorks Materials Engineering Database. Dassault Systèmes SolidWorks Corporation, 2026. Standard Aerospace and Structural Alloys Library.